Fabrication of 3D silicon anode by inkjet printing: Opportunities and challenges

Kinga Sztymela, Fabrice Rossignol, Marguerite Bienia, Nicolas Zapp, Kristian Nikolowski, Manuella Cerbelaud

To cite this version:

Kinga Sztymela, Fabrice Rossignol, Marguerite Bienia, Nicolas Zapp, Kristian Nikolowski, et al.. Fabrication of 3D silicon anode by inkjet printing: Opportunities and challenges. Journal of Energy Storage, 2024, 75, pp.109567. 10.1016/j.est.2023.109567 . hal-04575003

HAL Id: hal-04575003
https://unilim.hal.science/hal-04575003v1

Submitted on 15 Oct 2024

Journal of Energy Storage 75 (2024) 109567

Contents lists available at ScienceDirect

Journal of Energy Storage

journal homepage: www.elsevier.com/locate/est

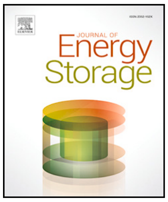

Research papers

Fabrication of 3D silicon anode by inkjet printing: Opportunities and challenges

Kinga Sztymela [a,*], Fabrice Rossignol [a], Marguerite Bienia [a], Nicolas Zapp [b], Kristian Nikolowski [b], Manuella Cerbelaud [a]

[a] *Univ. Limoges, CNRS, IRCER, UMR 7315, F-87000 Limoges, France*
[b] *Fraunhofer IKTS, Winterbergstraße 28, 01277 Dresden, Germany*

ARTICLE INFO

Keywords:
Li-ion batteries
Inkjet printing
Silicon
Anode
Printability
Inks

ABSTRACT

The pressing issue of climate change and the acceleration of global warming have prompted increased concerns about CO_2 emissions and the need for sustainable energy solutions. The transition to electric vehicles (EVs) is crucial in achieving a sustainable and greener future for our planet. Lithium-ion batteries (LIBs) are the most common storage energy systems used in the fabrication of EVs. However, further advancements are needed to improve their energy density, power density, safety, and cost. One promising approach is to replace conventional graphite anodes with silicon, offering higher capacity and environmental friendliness. This study explores the fabrication of three-dimensional (3D) silicon anodes using drop-on-demand (DOD) inkjet printing (IJP), a promising additive manufacturing technique. The formulation of stable aqueous inks for LIB anodes is presented, highlighting their potential for scalable production. The article addresses the difficulties encountered in developing printable inks for DOD IJP and assesses the electrochemical performance of these ink formulations. Inks containing carbon-coated silicon nanoparticles and PEDOT:PSS result in electrodes that attained the cutoff lithiation capacity of 2000 mAh $g_{AM}{}^{-1}$ with no observed capacity degradation over time. In contrast, anodes composed of pure silicon demonstrate a capacity decay after 75 cycles, proving the advantages of utilizing a Si/Carbon core-shell structure. The printability tests are presented, revealing the instabilities of the drop generation process, and the importance of particle surface chemistry. While it is possible to use IJP with the formulated anode inks, further optimization of the technology is necessary for practical implementation.

1. Introduction

In recent years, the climate crisis became one of the biggest concerns of humanity. Global warming is accelerating, posing a threat to both people and the environment [1]. The excessive emission of CO_2, as the primary greenhouse gas is the main responsible for this problem [2]. As pandemic restrictions were eased, and passenger and goods movements began to take up after a historic fall in 2020, worldwide CO_2 emissions from the transport sector rebounded in 2021, accounting for 37% of CO_2 emissions from end-use sectors [3]. Following the commitment from COP21 Paris Climate Agreement and COP26 Glasgow Climate Pact, major car manufacturers pledged to stop selling fossil-fuel vehicles by 2035, promoting transport electrification, and increasing demand for batteries' production [4,5].

Because of their high energy density to weight ratio, lithium-ion batteries (LIBs) are the most common energy storage systems used in the fabrication of electric vehicles (EVs) [6]. Although LIBs are state-of-the-art technology for EVs, their further development is anticipated, particularly in terms of energy density, power density, lifespan, safety, and cost [7].

The replacement of conventional graphite anode with silicon can significantly enhance the electrochemical characteristics of batteries. Silicon is one of the most promising materials for application in modern LIBs. Its extremely high theoretical specific capacity of 4200 $mAhg^{-1}$ is 11 times greater than that of graphite (372 mAh g^{-1}) [8]. Moreover, it offers low working potential (<0.4 V vs. Li/Li^+), being at the same time the second most abundant element on the Earth [9]. However, silicon undergoes large volumetric changes (>300%), while lithiation/delithiation processes. This results in the degradation of the electrode structure through isolation of active material, and constant growth of solid-electrolyte interphase (SEI) on the re-exposed particles surfaces, leading to poor cycling stability [10,11]. Several

---

* Corresponding author.
E-mail address: kinga.sztymela@unilim.fr (K. Sztymela).

https://doi.org/10.1016/j.est.2023.109567
Received 7 August 2023; Received in revised form 19 October 2023; Accepted 5 November 2023

strategies have been proposed to solve these problems, improving the electrochemical performance of silicon-based anodes [12,13]. Nanosized silicon materials, such as nanoparticles [14,15], nanowires [16,17], nanotubes [18], and three-dimensional porous structures [19], can withstand significant deformation strains without the mechanical fracture of the electrode. However, it was found that the high surface energy of nanoparticles promotes their merging during the cycling, forming a thick block after a few lithiation/delithiation processes, which causes an instantaneous capacity decay [20]. In order to address this issue, composite materials, which could buffer the volume changes and also increase the conductivity, were proposed [21]. One of the promising research fields is silicon/carbon core–shell structure. Carbon coating on the silicon particles' surface forms a conductive network, facilitating the electrons and ions transport. Furthermore, it can accommodate silicon structural changes and enhance SEI film stability [22–24].

Another promising strategy for the fabrication of silicon anodes with enhanced cycling stability is a three-dimensional (3D) electrode architecture [10]. Because of the higher surface area of such designs compared to conventional laminated structures, the lithiation stress is significantly reduced, eliminating the risk of mechanical disintegration [25]. Additionally, more active material may be loaded without sacrificing ion and electron kinetics. Therefore, 3D anodes are not subjected to the trade-off between energy density and power density [26,27].

Many additive manufacturing (AM) techniques have been proposed for the fabrication of modern 3D batteries' structures: direct ink writing (DIW) [28], fused filament fabrication (FFF) [29], stereolithography (SLA) [30], aerosol jet printing [31], and drop-on-demand (DOD) inkjet printing (IJP) [32]. DOD IJP offers many advantages over competing technologies. It allows for the deposition of a broad range of materials with high resolution and relatively high speed [33,34]. The fast fabrication may be particularly interesting for the industry, where batteries are produced at large scale. In this technique, the picoliter droplets (typically in the range of 1–1000 pL) of a functional ink are placed on a substrate, forming a pattern dictated by a CAD file [35,36]. Therefore, the printed design can be easily modified, bringing the benefits of scalability and cost-effectiveness. Additionally, it reduces material waste. Although DOD IJP is highlighted as an advantageous AM method for the fabrication of next-generation LIBs [37,38], the formulation of a printable ink may pose a challenge [39].

In this article, we present the formulation of stable water-based anode inks, specifically designed for DOD IJP, but also adaptable for other wet-processing techniques. The electrochemical properties of inkjet printable inks are analyzed to assess the effect of ink compositions. Additionally, we explore the possibilities and obstacles involved in creating 3D anode structures using the DOD IJP method. To assess printability, tests using various ink compositions are conducted, highlighting the significance of powder surface chemistry. Finally, we present microstructural analyses of the printed patterns.

2. Materials and methods

2.1. Anodes composition

For the formulation of anode functional inks, nanopowders of silicon (Si) (Nanomakers) and silicon coated by carbon (SiΩC) (Nanomakers) were used as active materials, and Super P Carbon Black (CB) (Alfa Aesar) was added as a conductive agent. Sodium carboxymethyl cellulose (CMC) of $M_w \sim 90000$ g/mol (DS = 0.7) (Sigma Aldrich), CMC of $M_w \sim 700000$ g/mol (DS = 0.9) (Sigma Aldrich), or poly(3,4-ethylenedioxythiophene)- poly(styrenesulfonate) (PEDOT:PSS) (Sigma Aldrich) were used as binders. The pH of CMC and PEDOT:PSS dissolved in DI-water is 7 and 1.7, respectively. NaOH (0.1M) was used to increase the basicity of PEDOT:PSS. The active material (0.2 g), conductive agent (0.1 g), and binder (0.1 g) in the ratio of 50:25:25 by weight were dispersed with deionized water (DI-water) and the dispersing agent Triton X-100 (Sigma Aldrich). In the following, the solvent and dispersing agent will be adapted for this ratio. In future works, it might be possible to increase the active material ratio; however, it would require adjustments to the entire ink formulation.

The composition of the slurries for tape-casting was adapted by reducing the solvent content. The ratio of active material to conductive agent to binder was kept fixed. To prevent the cracking of CMC-based anodes, Duramax B-1000 acrylic latex (Rohm and Haas) in the quantity of 9 wt% was added to the formulations. PEDOT:PSS was tested at its natural pH of 1.7, as well as at the pH level of 10. The compositions of anode slurries formulated for tape-casting are presented in Table 1.

2.2. Powder characterization

Particle size distributions of Si, SiΩC and CB powders were examined by Dynamic Light Scattering (DLS) technique using Zetasizer Nano ZS (Malvern Panalytical). The measurements were done on the diluted suspensions of the powders in DI-water (less than 0.1 wt% of powder).

The morphology of the powder particles was examined using transmission electron microscopy (TEM) JEOL 2010F (JEOL). Suspensions of nanoparticles in DI-water were loaded onto a grid support and left to dry before the examination.

Zeta potential versus pH was measured for Si, SiΩC, and CB powders using Zetasizer Nano ZS (Malvern Panalytical). To adjust pH, NaOH (0.1 M) and HCl (0.1 M) were used.

The surface chemistry of Si and SiΩC was analyzed using Nicolet 6700 FTIR spectrometer (Thermofisher).

2.3. Ink preparation

The optimal amount of the dispersing agent was determined by viscosity measurements with the rheometer Fluidicam (Formulaction). A set of suspensions (1.5 wt% of powder in DI-water) with various concentrations of the dispersant was analyzed.

Binders were dissolved in DI-water by magnetic stirring. Si or SiΩC and CB were dispersed with DI-water and the optimal amount of Triton X-100 using the high-speed disperser. Afterward, both of the mixtures were combined and put in an ultrasonic bath for a minimum of 1 h.

2.4. Ink characterization

The inverse of the Ohnesorge number referred to as the Z value (Z=1/Oh) is commonly used in most commercial DOD printing systems as the indicator of printability [40]. Z value is given by the formula:

$$Oh = \frac{\eta}{\sqrt{\gamma \rho a}}, \tag{1}$$

where η, γ, ρ and a are the dynamic viscosity, surface tension, density, and characteristic length respectively [41].

Generally, when 1<Z<10, ink is considered printable. For Z<1, the viscosity is too high, preventing the ejection. On the other hand, when Z is greater than 10, additional tiny droplets called satellites are formed next to the main drop, resulting in poor printing quality [34].

To determine the Z values of the formulated inks, the viscosity, surface tension, and density were measured. The viscosity as a function of the shear rate was evaluated using Discovery Hybrid Rheometer HR-2 (TA Instruments) with double wall concentric cylinders steel geometry (inside cup diameter 40 mm, inner cylinder height 21 mm). The surface tension was tested by the tensiometer DCAT21 (Dataphysics) with a platinum Wilhelmy plate. To measure the density, a known volume of ink was weighted on a precision scale (Denver). For all the tests, the temperature was set to 20 °C. The stability of the anode inks was assessed using Turbiscan LAB (Formulaction) and sedimentation tests. For the sedimentation tests, samples of each ink were filled into test tubes and placed on a stable surface. The test tubes were then left undisturbed for 24 h. During this time, the settling behavior was visually examined.

Table 1
Compositions of anode slurries used for fabrication of tape-casted electrodes.

Nomenclature	Active material	Binder	Conductive agent	Additives
SiΩ2126C_CMC_90k	45.5 wt% SiΩ2126C	22.75 wt% CMC M_w 90 000	22.75 wt% CB	9 wt% Latex Duramax B-1000
SiΩ2126C_CMC_700k	45.5 wt% SiΩ2126C	22.75 wt% CMC M_w 700 000	22.75 wt% CB	9 wt% Latex Duramax B-1000
Si_CMC_700k	45.5 wt% Si	22.75 wt% CMC M_w 700 000	22.75 wt% CB	9 wt% Latex Duramax B-1000
SiΩ2126C_PEDOT_nat	50 wt% SiΩ2126C	25 wt% PEDOT:PSS (natural pH)	25 wt% CB	–
SiΩ2126C_PEDOT_mod	50 wt% SiΩ2126C	25 wt% PEDOT:PSS (modified pH)	25 wt% CB	–
Si_PEDOT_nat	50 wt% SiΩ2126C	25 wt% PEDOT:PSS (natural pH)	25 wt% CB	–

2.5. Battery assembly and electrochemical testing

To evaluate how the ink formulations affect the anode's performance, electrochemical tests were conducted on tape-casted electrodes. Casted silicon anodes were heated at 80 °C for 16 h in a vacuum to remove adhesive moisture. Then, three specimens per anode type were die-cut (12 mm diameter) and used for the construction of CR2032 coin cells with metallic lithium counter electrode (14 mm diameter), two borosilicate glass fiber separators, and 150μL liquid electrolyte (0.9 M $LiPF_6$ in 45 vol.-% ethylene carbonate, 45 vol.-% dimethyl carbonate, 10 vol.-% fluoroethylene carbonate). The cells were temperature-equilibrated for 22 h at 30 °C before cycling them with a constant current of 0.05C four times (formation) and subsequently 100 times with 0.2C using cutoff voltages of 10 mV (lithiation) and 1.0 V (delithiation) with a BaSyTec cell test system (Basytec GmbH, Asselfingen, Germany). Between each cycle, 5 min open circuit voltage was recorded. The charging rate was calculated assuming a maximum capacity of the silicon active material of 3580 mAh g^{-1}, whereas lithiation was stopped at 2000 mAh g^{-1} for enhanced reversibility, in case the cutoff voltage criterion was not met.

2.6. Inkjet printing

Printing and printability tests were performed using piezoelectric drop-on-demand inkjet printer CeraPrinter X-Serie (Ceradrop) with the printhead Dimatix SClass SL (Fujifilm) with 128 nozzles of a nominal droplet volume 80 pL and the diameter 50 μm. It is recommended for this printer to formulate inks with a viscosity between 5 and 20 mPas, a surface tension from 30 to 35 mN/m, and a particle size lower than 1 μm. Before transferring inks to the cartridge, each was passed through GF/C glass microfiber 1.2 μm filters (Whatman), to eliminate possible large particles. Fabrication was done onto Cu foil, with the possibility of heating the substrate holder to 60 °C. The working distance (distance between the nozzle and the substrate) was fixed at 500 μm.

A trapezoidal voltage waveform (see Figure S1) including a rise time t_{rise}, peak hold at the maximum voltage V during a dwell time t_{dwell}, and drop to 0 V during a time t_{fall} is supplied to the piezoelectric material to push and eject the liquid. The electric pulse was adjusted separately for each ink through a trial-and-error approach until a stable drop generation process was obtained. Due to printhead limitations, the maximum applied voltage is 120 V, and the total time cannot exceed 15 μs. The behavior of inks exiting the nozzles was registered by a stroboscopic image acquisition system.

3. Results

3.1. Powders characterization

Before formulating the ink, it is crucial to take into account the size of the powder particles. To avoid nozzle clogging during printing, it is advisable to ensure that the diameter of the nozzle is at least 50 times greater than the particle size [42]. Therefore, in order to meet the specifications of the printheads used in this study, powder particles should have a size smaller than 1 μm. Otherwise, powders may require grinding. In addition, it is essential to prevent the formation of aggregates larger than 1μm, which can block the nozzles.

TEM observations of Si and SiΩC particles (Fig. 1a,c) do not show a difference between the two powder grades. Spherical primary particles of the diameter 40 nm aggregate as strings of a few particles. Fig. 1b,d illustrate the particle size distribution of Si and SiΩC, obtained with the DLS technique. The average hydrodynamic particle size for both powders was around 200 nm. Comparing this value with the size of the primary particles observed by TEM (Fig. 1a,c), it was concluded that the measured value of 200 nm corresponds to particle aggregations found in suspension.

The TEM analysis (Fig. 1e) of CB reveals the presence of aggregates composed of fused spherical particles, measuring approximately 40 nm. On the other hand, the granulometric measurement (DLS technique) (Fig. 1f) indicates an average hydrodynamic particle size of around 500 nm, which refers to the aggregate size attainable in suspension.

The results indicated that the powder particle size was appropriate for IJP. However, to eliminate any potential large aggregates, all the inks were filtered before the printing process.

3.2. Ink formulation

In the first step of anode ink preparation, zeta potential versus pH was measured for Si, SiΩC, and CB powders, which enabled establishing which range of pH is the most suitable for the formulation. Plots in Fig. 2 demonstrate a significant negative zeta potential for all powders when the pH values exceed 6. Naturally, the diluted suspensions prepared with only these powders were in this range of pH stable, but it is important to acknowledge the presence and influence of a binder. When CMC was introduced into the suspension, the pH remained relatively unchanged, having no significant impact on the surface charge of the particles. In this case, the pH of the inks prepared with CMC was at approximately 6.7. However, when the PEDOT:PSS binder was used, the suspension's pH drastically decreased to approximately 3.2. This resulted in a notable decrease in the zeta potential of the powders, subsequently leading to the aggregation of particles in the dilute suspension. This was due to the acid nature of the PEDOT:PSS, which has a pH of 1.7. To address this issue, some formulations were developed by adding NaOH (0.1M) solution to elevate the pH, which in turn increased the absolute zeta potential of the particles. As a consequence, the final pH of inks formulated with PEDOT:PSS was approximately 10.

Although the suspensions of Si and SiΩC in water exhibited high stability, this only applied to highly diluted suspensions (for instance, 0.5 wt% of powder in water). When increasing the amount of Si or SiΩC, agglomerates were formed, indicating unstable dispersion. In

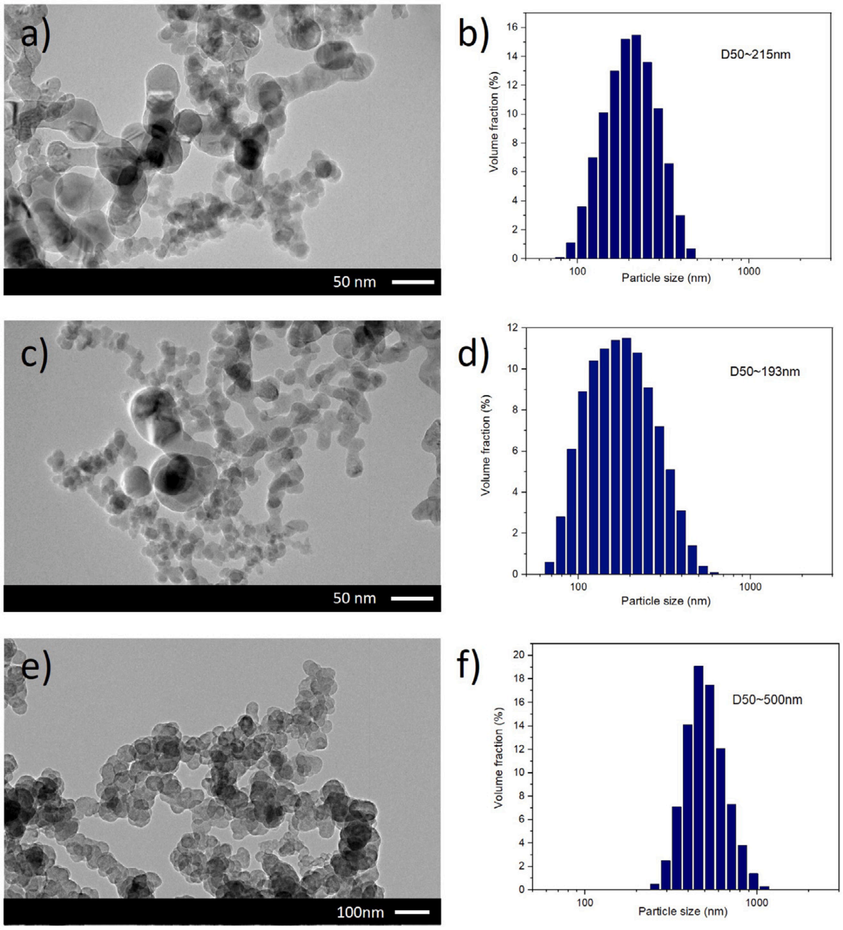

Fig. 1. Morphological characterization and particle size distributions of powders: (a), (c), (e) TEM images of Si, SiΩC, and CB powders, respectively; (b), (d), (e) Particle size distribution obtained with DLS technique of Si, SiΩC, and CB powders, respectively.

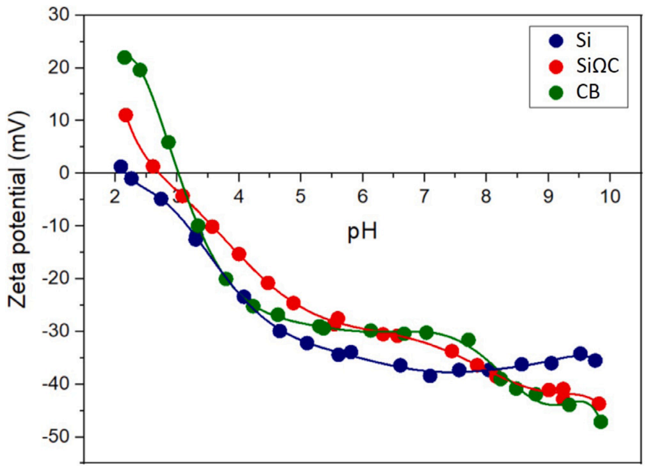

Fig. 2. Zeta potential of Si, SiΩC, and CB, as a function of pH measured using Zetasizer Nano ZS.

addition, particles can also display hydrophobic characteristics, causing the particles to repel water and agglomerate [43]. To ensure that particles remain discrete and to help overcome the hydrophobicity, a dispersing agent Triton X-100 was added to the formulation. The surfactant was selected via simple sedimentation experiments. Triton X-100 showed satisfactory results for all powders, Si, SiΩC, and CB. Using one kind of dispersant helps to avoid the risk of unwanted interactions between ink components.

The optimal amount of the dispersing agent was evaluated by viscosity measurements using the rheometer Fluidicam. The results are presented in Fig. 3. As the concentration of dispersing agent increases, the viscosity of the dispersion should decrease, indicating better dispersion of powder particles in the water. The concentration at which the viscosity reaches a minimum represents the optimal amount of dispersing agent required to achieve stable dispersion. The optimal concentration values were 10 wt%, 30 wt%, and 50 wt% for SiΩC, Si, and CB, respectively. The use of the high amount of Triton X-100 might be surprising, but it can be rationalized by the need to evenly coat the extensive surface area of the nanoparticles in order to prevent clumping. Similar observations have been reported in previous studies [44].

In our study, numerous inks were prepared with various solvent-to-powders ratios, and they were optimized using a trial-and-error method. Here, we present only examples of formulations, which were optimal in terms of stability and printability. It should be noted that inks with CMC of M_w~700 000 g/mol were also formulated but their high viscosity made them unsuitable for IJP. Therefore, they were not considered for further analysis in this study.

The composition of formulated inks is presented in Table 2. For ease, in this work, we denoted the formulations as shown in the first column, i.e. INK_SiΩC_CMC, and INK_SiΩC_PEDOT, INK_Si_CMC, INK_Si_PEDOT.

3.3. Inks characterization

Table 2 presents the rheological characteristics and calculated Z values for anode inks. The viscosity values correspond to a shear rate

Table 2
Composition and characteristics of formulated anode inks designed for IJP.

Nomenclature	Composition	Solvent	Surface tension (mN/m)	Viscosity at 100^{-1} (mPa.s)	Density (g/ml)	Z	pH
INK_SiΩ2126C_CMC	SiΩ2126C+CB+CMC	DI-water	32.1	3.3	0.74	~10	6.7
INK_SiΩ2126C_PEDOT	SiΩ2126C+CB+PEDOT:PSS	DI-water+NaOH	32.3	8.2	0.76	~4	10.1
INK_Si_CMC	Si+CB+CMC	DI-water	32.1	3.4	0.72	~10	6.7
INK_Si_PEDOT	Si+CB+PEDOT:PSS	DI-water+NaOH	32.3	4.5	0.75	~8	10.2

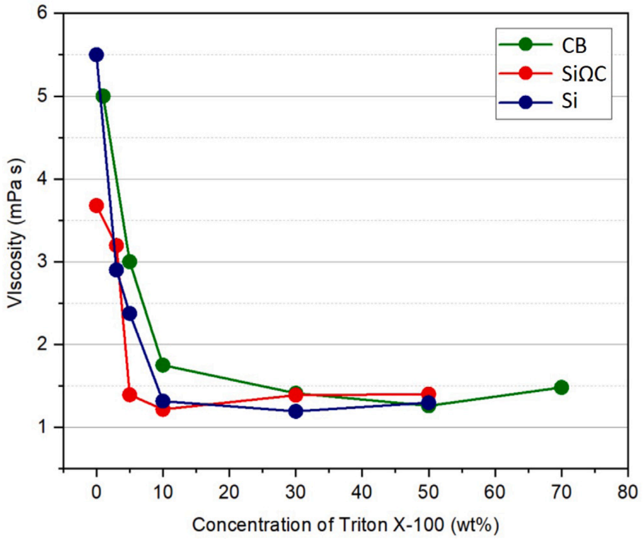

Fig. 3. Determining the optimal dispersing agent concentration: viscosity as a function of Triton X-100 concentration for Si, SiΩC, and CB powders (1.5 wt% of powder in DI-water), measured with the rheometer Fluidicam.

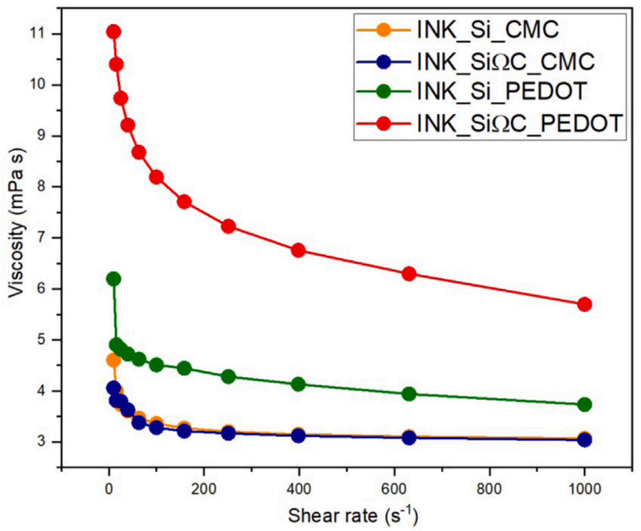

Fig. 4. Viscosity as a function of shear rate for INK_SiΩC_CMC, INK_SiΩC_PEDOT, INK_Si_CMC, INK_Si_PEDOT inks, measured with Discovery Hybrid Rheometer HR-2.

of 100 s^{-1}, while Fig. 4 demonstrates the viscosity variations across the range of 10 to 1000 s^{-1}.

Despite the viscosities of INK_SiΩC_CMC, INK_Si_CMC, and INK_Si_PEDOT being lower than the required threshold, the Z values for these inks were within the printable range.

For each ink, a slightly shear-thinning behavior was observed, with INK_SiΩC_PEDOT exhibiting the most noticeable effect. The decrease in viscosity with increasing shear rate ensures a smooth flow of the ink through the nozzle during the printing process.

The stability of the anode inks was evaluated using Turbiscan LAB and sedimentation tests (see Figure S2). Although the stability of formulated inks after 24 h might be considered unsatisfactory, it was sufficient for IJP. During the first hour, only minimal changes were observed in the suspensions.

3.4. Electrochemical analysis

To evaluate how the ink formulations affect the anode's performance, electrochemical tests were conducted on tape-casted electrodes. Moreover, a formulation with a different kind of CMC was developed. For IJP, CMC with a relatively low molecular mass of 90 000 g/mol was used due to the need for low viscous ink. In literature, it was indeed demonstrated that higher molecular weight of CMC may result in more favorable electrochemical performance of silicon anode [45]. For the sake of comparison, anodes with CMC of M_w~700 000 g/mol were also fabricated and electrochemically tested.

As previously discussed, in order to achieve a stable suspension of inks formulated with PEDOT:PSS as a binder, it was necessary to adjust its pH. This modification resulted in different polymer structures. At low pH (natural PEDOT:PSS pH), the polymer created a connected network, while at the high value (pH ~ 10), separated clusters were observed (refer to Figure S3). These observations might suggest that the modified pH level negatively impacts the electrochemical performance of the anode. The disconnected structure of an electrode could hinder efficient electron and ion transport, contributing to lower capacity, reduced cycling stability, and shorter overall battery lifespan. Therefore, the anode formulated with PEDOT:PSS as a binder, but without the pH adjustment was also tested.

The compositions of tape-casted anodes are presented in Table 1.

PEDOT:PSS-based samples performed best, attaining the cutoff lithiation capacity of 2000 mAh $g_{AM}{}^{-1}$ right after the formation (Fig. 5). The pH variation of the PEDOT:PSS solution did not significantly affect the results. The carbon-silicon composite active material SiΩC did not show capacity fading, in contrast to the silicon-based specimen, whose capacity declined from the 75th cycle onward by circa 20% at cycle 104. The sudden drop can be attributed to the limitation of cycling to 2000 mAh $g_{AM}{}^{-1}$. During the initial 75 cycles, a portion of the silicon was irreversibly consumed, but it was subsequently replenished with fresh silicon due to a significant unused capacity range between 2000 and 3580 mAh g^{-1}. The remarkable electrochemical performance exhibited by anodes formulated with PEDOT:PSS in comparison to those incorporating CMC can be attributed to the nature of the binder. PEDOT:PSS is an electrically conductive polymer, improving the electron transport within the electrode. This enhanced conductivity allows for better utilization of the active silicon material, leading to improved electrochemical performance. Moreover, PEDOT:PSS possesses good flexibility, which helps to accommodate the volume expansion of silicon without severe structural damage. This property could reduce the mechanical strain on the electrode, maintaining its structural integrity and prolonging cycle life.

These findings align with the observations of Escamilla-Perez et al. [24], which proved that carbon-coated silicon anodes offer improved stability. The carbon coating acted as a protective layer, mitigating the detrimental effects of volume expansion and improving the stability and structural integrity of the electrode. Furthermore, the carbon

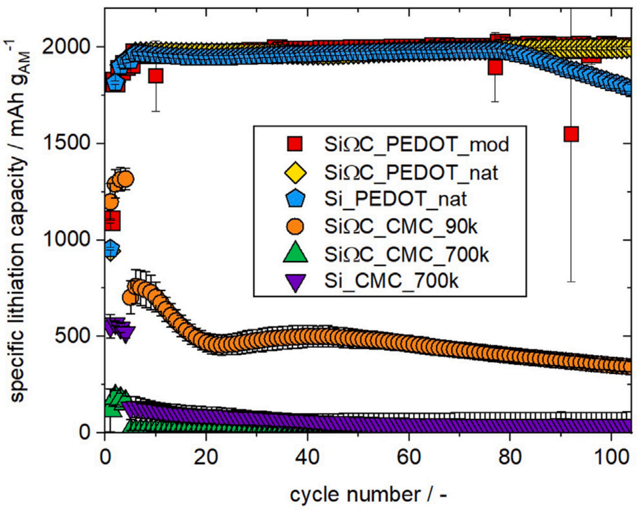

Fig. 5. Specific discharge capacity versus cycle number at 0.05C (4 initial cycles), and 0.2C (100 cycles) for tape-casted anodes. The measurements were performed at 30 °C. SiΩC_PEDOT_mod - SiΩC anode with PEDOT:PSS at modified pH of 10; SiΩC_PEDOT_nat - SiΩC anode with PEDOT:PSS at natural pH of 1.7; Si_PEDOT_nat - Si anode with PEDOT:PSS at natural pH of 1.7; SiΩC_CMC_90k - SiΩC anode with CMC of $M_w \sim 90000$; SiΩC_CMC_700k - SiΩC anode with CMC of $M_w \sim 700000$; Si_CMC_700k - Si anode with CMC of $M_w \sim 700000$.

coating likely led to the minimized formation of SEI, creating a barrier between the silicon and electrolyte. This allowed for better electrolyte penetration and improved cycling stability.

CMC/Latex-based samples exhibited much lower lithiation capacities, whereas the low molecular weight CMC reached higher values. This might result from a diffusion limitation due to the encapsulation of active material in the lowly lithium-ion conducting binder, which is evidenced by the capacity loss upon the increase of the lithiation rate. These findings probably result from the necessary addition of latex. CMC, which is commonly used as binder material for electrodes, might thus still be suitable as binder for silicon anodes. Moreover, it is important to take into account the presence of the high amount of Triton X-100, which could also contribute to the reduction of lithium ion diffusion. However, it should be acknowledged that these electrodes were fabricated only for comparison purposes between different ink formulations designed for IJP. When appropriately tailored, CMC-based anodes built of Si or SiΩC nanopowders from Nanomakers can provide satisfactory electrochemical properties [46].

3.5. *Printability tests*

Although the cycling performance of electrodes formulated with CMC was poor, the ink formulations corresponding to these electrodes were considered in the subsequent part of the study. As mentioned earlier, the unsatisfactory electrochemical results might be attributed to the presence of latex. However, latex could be excluded from the ink compositions designed for inkjet printing applications. In IJP technique, the material is deposited in the form of small droplets placed adjacent to each other. Consequently, the drying conditions for the printed structure differ from those of tape-casted electrodes. This controlled approach gives sufficient time for the ink to dry and reduces the build-up of stress within the deposited layers, minimizing the likelihood of cracking. Therefore, the addition of latex may be unnecessary for the inks tailored for IJP, and the printability tests were conducted on all the formulated inks (see Table 2).

3.5.1. *Inks with SiΩC*

The drop generation process was recorded frame by frame using the optimal parameters of $t_{rise} = 2\,\mu s$, $t_{dwell} = 5\,\mu s$, $t_{fall} = 2\,\mu s$, V = 75 V, and $t_{rise} = 5\,\mu s$, $t_{dwell} = 0\,\mu s$, $t_{fall} = 5\,\mu s$, V = 50 V for INK_SiΩC_CMC (Fig. 6a), and INK_SiΩC_PEDOT (Fig. 6b), respectively.

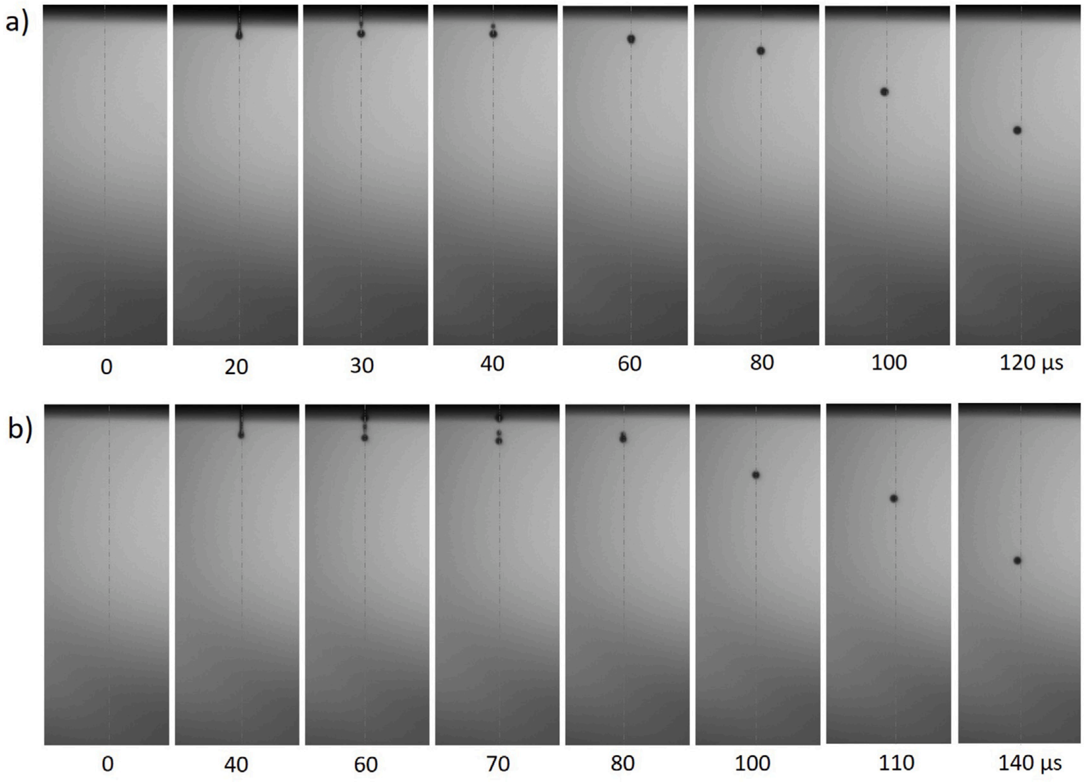

Fig. 6. Drop generation process with optimal parameters registered frame by frame for: (a) INK_SiΩC_CMC; (b) INK_SiΩC_PEDOT. The dotted line indicates the nozzle central axis.

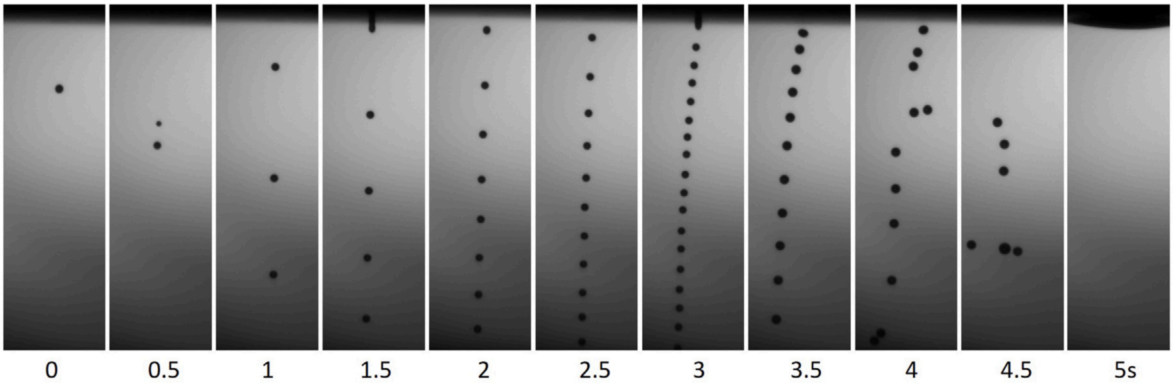

Fig. 7. Ejection process of INK_SiΩC_CMC when increasing jetting frequency from 100 Hz to 1000 Hz.

In both cases, the liquid flowed out from the nozzle, creating the main droplet with an attached filament. Subsequently, the filament was detached, and its tail end formed a second drop, which speeded up, and the two merged together. While successful jetting was achieved, there was a slight deviation of the droplet's path from the nozzle central axis (indicated by dotted lines), potentially leading to poor printing quality. Furthermore, this deviation was unpredictable. The droplets experienced varying degrees of displacement in both directions. The deviation illustrated in Fig. 6 was minor initially, but it worsened as the printing process continued (refer to Figure S4).

Optimizing the jetting frequency, a correlation between the frequency value and nozzle clogging issue was uncovered. Fig. 7 displays the step-by-step ejection process of INK_SiΩC_CMC, utilizing the optimal electric pulse, as the frequency increases. Initially (at 0 μs), a frequency of 100 Hz was employed, which was promptly raised to 1000 Hz. This immediate increase in frequency resulted in instant instability of the jetting process, and after 5 s, the ink could no longer be ejected. The experiment conducted with INK_SiΩC_PEDOT exhibited a similar phenomenon but with a shorter ejection duration. In this instance, the nozzle became clogged after only 3 s.

The relationship between the jetting frequency and the percentage of clogged nozzles is presented in Figure S5.

Applying low values of the jetting frequency allowed for the deposition, although the ejection time was limited. Additionally, this significantly impacted the processing time. To give an idea, considering the deposition of a single layer of 10 × 10 mm, a decrease in the frequency from 1000 to 100 Hz causes an increase in the printing time from 5 to 50 min. Therefore, IJP loses its advantage of being a fast deposition method.

To sum up, the ejection of anode inks formulated with SiΩC was possible, but the drop generation process was not stable. Several assumptions were made to explain the origins of the instabilities.

Large agglomeration of powder particles could fully or partially clog the nozzles. Agglomerates were a barrier to fluid flow, blocking it or deviating the drop trajectory.

A thin multilayer of ink could progressively deposit on the surface of the nozzles. Initially, ejection was possible, but with time, orifices get smaller, until they were fully clogged. When the deposited material was not homogeneously distributed on the nozzles plate, non-symmetric jetting might be observed. Moreover, a part of the layer could be detached and displaced during the process, blocking the nozzles. This explanation has been proposed by Li et al. [47]. It is likely that high jetting frequency promoted the detachment of the deposited materials, leading to subsequent blockage of the orifices.

The deposited material might alter the shape of the meniscus formed by the ink and air. This could lead to the entrapment of air and encourage air bubbles to stick to the inside surfaces of the printhead. As a result, the ejection might be disrupted or blocked, which was also promoted by high jetting frequency [48].

Viscoelasticity might be another reason for the drop trajectory's unpredictable deviation [49]. Each of the tested inks was composed of a polymeric binder, necessitating consideration of the behavior of polymers during the jetting process. Prior to printing, when no stress was applied, the polymeric chains existed in a coiled configuration. As the ink exited the nozzle, these chains underwent a transformation into a stretched state. Subsequently, upon detachment of the ink droplet, the polymeric chains returned to their coiled state. This phenomenon implied that within a droplet, the polymeric chains reorganized their structure, potentially causing disturbances in the trajectory.

3.5.2. *Inks with Si*

Although the inks prepared with pure Si exhibited satisfactory stability, their ejection was impossible, even when applying the jetting frequency of 1 Hz. All the nozzles became clogged immediately after starting the printing. As the only difference between these inks and those prepared with SiΩC was the type of active material, it was assumed that Si nanoparticles were the main responsible for the issue. To confirm that, another ink with 50% less silicon powder than the initial ink was tested, and its behavior was registered frame by frame (Fig. 8).

Initially, ejection was possible, but the drop generation process was unstable. Within only 3 s, all the nozzles became clogged. Consequently, even with a reduced amount of active material in the ink, the problem of clogging persisted, rendering printing impossible. These outcomes confirmed that the issues were attributed to the presence of pure silicon nanoparticles.

One hypothesis that could explain the clogging problem was the formation of air bubbles directly inside the printheads, preventing fluid flow. Si nanoparticles react with water to produce silicon dioxide, and hydrogen gas [50]. Generated gas entrapped inside the printheads could hinder the ejection. To verify it, printability tests were performed with the same ink that had been stored for a period of 2 months. Although after this time, the reaction kinetic should be much lower, the same behavior was observed. All the nozzles were immediately clogged, and the ejection was impossible.

To further investigate the origin of the problem, the surface chemistry of both Si and SiΩC powders was compared by FTIR analysis. FTIR spectra are presented in Fig. 9a.

The absorbance band between 2000 and 2200 cm^{-1} correspond to SiH_x stretching modes, and the peak at 2256 cm^{-1} is attributed to O_ySiH_x species [51]. These groups were observed only for pure Si and are the evidence of partial surface oxidation, the formation of the native SiO_2 layer. Carbon on the Si surface, a well-known reducing media, most likely converts the SiO_2 layer into Si or SiO_x layer (with $x < 2$) [46]. It is possible that these functional groups could create chemical bonds with hydroxyl groups present on the metallic surface of the nozzle. A schematic representation of the bonding is shown in Fig. 9b.

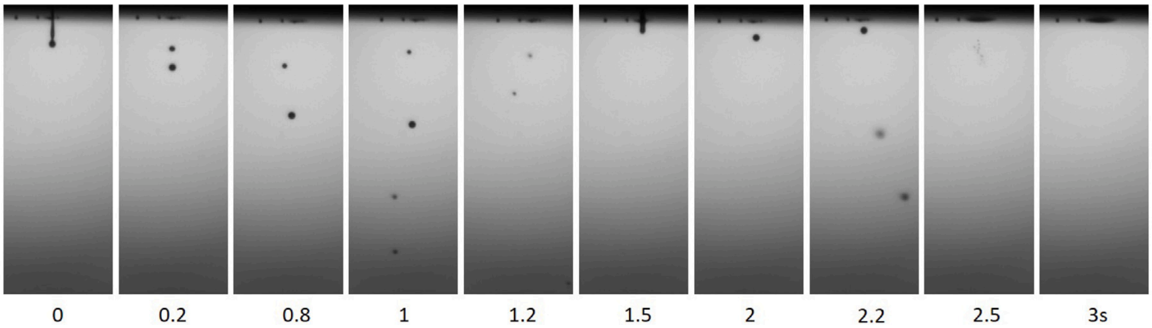

Fig. 8. The ejection of anode ink formulated with CMC and decreased amount of Si particles.

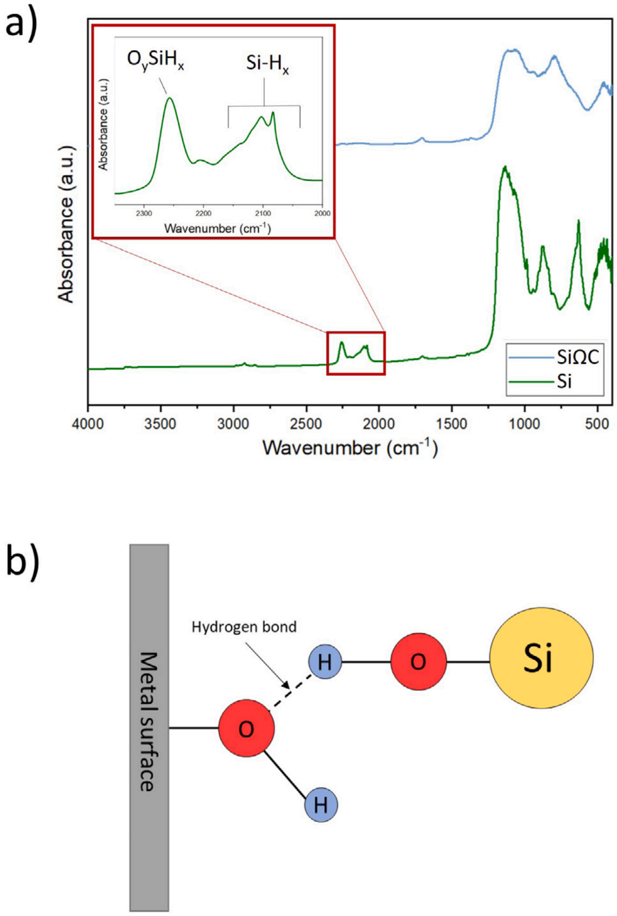

Fig. 9. (a) FTIR spectra of Si and SiΩC powders, (b) Schematic representation of hydrogen bond between Si particle and metal surface possibly causing the ejection issue.

3.6. Microstructural characterization

Despite the unstable ejection process, which posed a challenge to printing efficiency, the deposition of anode inks was demonstrated. Because of unstable jetting conditions and not reproducible results, inkjet printing was performed using only one nozzle. Both INK_SiΩC_CMC and INK_SiΩC_PEDOT inks were tested, but only the structures created with the former are presented since the results were analogous. Depositions of anode inks were performed on the copper foil.

To successfully print thin layers, the spacing between deposited droplets and the temperature of the substrate holder had to be optimized (refer to Figure S6). The diameter of a single splat deposited on the foil was around 50 μm, and squares of 1 × 1 cm were printed as trials.

Overlapping of droplets by 25 μm and the temperature of the substrate holder set to 50 °C yielded the best results with relatively high material loading being homogeneously distributed on the foil. By repeating the pattern multiple times, more uniform structures could be obtained. However, the nozzles became clogged during the printing process, which limited the printing time.

It is noteworthy that the deposition of anode layers containing CMC using IJP was accomplished without experiencing cracking issues. The incorporation of latex, which was suspected to have a detrimental impact on electrochemical performance, proved unnecessary for ink formulation designed for IJP.

Although the printing of thin layers was possible, it was challenging to fabricate samples, which could be electrochemically characterized. The process was not reproducible, with the issue of nozzle clogging repeatedly appearing.

To investigate the possibilities of 3D structure fabrication using IJP, an experiment was conducted to print anode pillars by depositing individual drops on top of one another.

Fig. 10a presents single splats of INK_SiΩC_CMC ink deposited without heating of the substrate, while Fig. 10b shows the same pattern printed with the substrate temperature of 50 °C. The elevated temperature decreased drying time, resulting in a more homogeneous structure with powders uniformly distributed within splats. When no heating was applied, more material was loaded on the edges. This phenomenon is called the coffee-ring effect, and it is an issue that frequently arises during the drying of particle-laden droplets. The non-uniform evaporation flux at the air–liquid interface of the sessile droplet, which is observed to be larger along the three-phase contact line, is what drives this ubiquitous process. The larger liquid loss at the edges is replenished by the fluid from the drop center. The particles are then driven to the contact line by an evaporation-induced flow, and as the solvent completely evaporates, a pattern in the shape of a ring emerges [52]. Additionally, some of the splats fused with each other, leading to a disordered arrangement. Therefore, heating the substrate is beneficial for printing well-defined structures.

Fig. 10c shows the same pattern repeated 3 times with the heating of the substrate. The accuracy of the drop positioning was insufficient to build the intended 3D shape.

4. Conclusions

In conclusion, we presented the formulation of stable water-based anode inks, specifically designed for IJP, but also adaptable for other wet-processing techniques.

Anodes fabricated with PEDOT:PSS binder exhibited excellent performance. The electrodes containing carbon-coated silicon nanoparticles and PEDOT:PSS achieved a cutoff lithiation capacity of 2000 mAh $g_{AM}{}^{-1}$ with no observed capacity degradation over time. In contrast, anodes composed of pure silicon demonstrate a capacity decay after

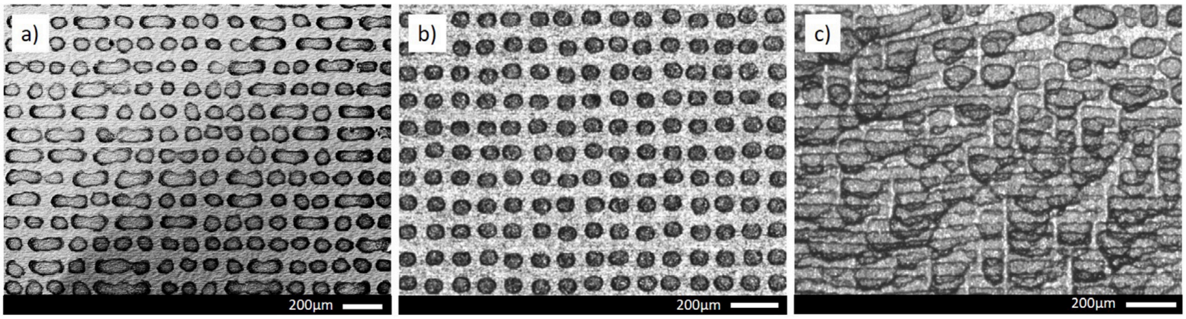

Fig. 10. Single splats of INK_SiΩC_CMCCMC: (a) without heating of the substrate, (b) with the substrate temperature of 50 °C, (c) after 3 passes of printing with the substrate temperature of 50 °C.

75 cycles, proving the advantages of utilizing silicon/carbon core–shell structure.

Printability tests revealed the instabilities of the drop generation process and the importance of particle surface chemistry. While inks formulated with SiΩC were capable of being ejected, the printing process itself proved to be unstable. This instability could be attributed to various factors such as the accumulation of large agglomerations of powder particles leading to nozzle clogging, the gradual buildup of a thin multilayer of ink on the nozzle's surface, entrapment of air bubbles, or the viscoelastic nature of the inks. Furthermore, our findings demonstrated a direct correlation between the jetting frequency value and the occurrence of nozzle clogging. Higher jetting frequencies were found to promote nozzle clogging. Consequently, the deposition of anode inks became feasible by utilizing lower jetting frequencies, but this came at the expense of losing the advantage of fast deposition associated with IJP.

While exhibiting satisfactory stability, inks formulated with pure silicon were unable to be ejected, even at extremely low jetting frequencies. Two possible explanations for this issue were the generation of air bubbles within the printheads, or the chemical bonding between the surface of silicon nanoparticles and the hydroxyl groups on the metallic surface of the nozzle.

Despite facing challenges with the ejection process, we successfully achieved the deposition of anode inks formulated with SiΩC. By optimizing the printing parameters, we were able to obtain uniform thin layers.

It is noteworthy that the deposition of anode layers containing CMC using IJP was accomplished without experiencing cracking issues, contrary to the tape-casted electrodes. Therefore, the addition of latex, which was suspected to have a detrimental impact on electrochemical performance, proved unnecessary for ink formulation designed for IJP.

However, when attempting to build 3D structures, we encountered limitations in the accuracy of drop positioning, which hindered the desired outcome. To address these issues, further refinement and optimization of the technology are necessary, particularly in mitigating nozzle clogging.

One potential solution is the application of non-adsorbing coatings on the surface of the nozzles. This could help minimize the formation of hydrogen bonds between the ink particles and the nozzle surface, thereby reducing clogging. Additionally, the implementation of a cleaning unit designed to unblock the nozzles during the printing process could contribute to a more stable and reliable process. In addition to these adjustments, alternative printing technique such as acoustic inkjet printing could also be envisaged. This nozzle-free method could indeed help mitigate the clogging issue.

Overall, further optimization efforts are essential to enhance printing accuracy and stability, allowing for the successful fabrication of 3D structures using silicon anode inks.

Declaration of competing interest

The authors declare that they have no known competing financial interests or personal relationships that could have appeared to influence the work reported in this paper.

Data availability

No data was used for the research described in the article.

Acknowledgments

This project has received funding from the European Unions's Horizon 2020 research and innovation programme under grant agreement N° 875029. This output reflects only the author's view and the European Union cannot be held responsible for any use that may be made of the information contained therein. The authors further acknowledge Nanomakers for providing silicon powders.

Appendix A. Supplementary data

Supplementary material related to this article can be found online at https://doi.org/10.1016/j.est.2023.109567.

References

[1] B. Pandey, K.K. Choudhary, Air pollution: role in climate change and its impact on crop plants, in: Climate Change and Agricultural Ecosystems, Elsevier, 2019, pp. 211–247, http://dx.doi.org/10.1016/B978-0-12-816483-9.00009-8.

[2] EPA United States Environmental Protection Agency, Overview of greenhouse gases, 2022, https://www.epa.gov/ghgemissions/overview-greenhouse-gases. (Accessed 18 December 2022).

[3] Transport, IEA, Paris, IEA 2022, 2022, https://www.iea.org/reports/transport. (Accessed 18 December 2022).

[4] M.A. Tamor, E.B. Stechel, Electrification of transportation means a lot more than a lot more electric vehicles, iScience 25 (6) (2022) 104376, http://dx.doi.org/10.1016/j.isci.2022.104376.

[5] UN-FCCC, COP26 the Glasgow climate pact, United Nations International Framework Convention on Climate Change (2021), 2022, https://ukcop26.org/wp-content/uploads/2021/11/COP26-Presidency-Outcomes-The-Climate-Pact.pdf. (Accessed 18 December 2022).

[6] S. S. Rangarajan, S.P. Sunddararaj, A. Sudhakar, C.K. Shiva, U. Subramaniam, E.R. Collins, T. Senjyu, Lithium-ion batteries—The crux of electric vehicles with opportunities and challenges, Clean Technol. 4 (4) (2022) 908–930, http://dx.doi.org/10.3390/cleantechnol4040056.

[7] M. Armand, P. Axmann, D. Bresser, M. Copley, K. Edström, C. Ekberg, D. Guyomard, B. Lestriez, P. Novák, M. Petranikova, et al., Lithium-ion batteries-Current state of the art and anticipated developments, J. Power Sources 479 (2020) 228708, http://dx.doi.org/10.1016/j.jpowsour.2020.228708.

[8] C.M. Hayner, X. Zhao, H.H. Kung, Materials for rechargeable lithium-ion batteries, Annu. Rev. Chem. Biomol. Eng. 3 (2012) 445–471, http://dx.doi.org/10.1146/annurev-chembioeng-062011-081024.

[9] L. Sun, Y. Liu, R. Shao, J. Wu, R. Jiang, Z. Jin, Recent progress and future perspective on practical silicon anode-based lithium ion batteries, Energy Storage Mater. 46 (2022) 482–502, http://dx.doi.org/10.1016/j.ensm.2022.01.042.

[10] W.-F. Ren, Y. Zhou, J.-T. Li, L. Huang, S.-G. Sun, Si anode for next-generation lithium-ion battery, Curr. Opin. Electrochem. 18 (2019) 46–54, http://dx.doi.org/10.1016/j.coelec.2019.09.006.

[11] Y. Yang, S. Wu, Y. Zhang, C. Liu, X. Wei, D. Luo, Z. Lin, Towards efficient binders for silicon based lithium-ion battery anodes, Chem. Eng. J. 406 (2021) 126807, http://dx.doi.org/10.1016/j.cej.2020.126807.

[12] X. Song, X. Wang, Z. Sun, P. Zhang, L. Gao, Recent developments in silicon anode materials for high performance lithium-ion batteries, J. Mater. Matters 8 (2016).

[13] W. Tao, P. Wang, Y. You, K. Park, C.-Y. Wang, Y.-K. Li, F.-F. Cao, S. Xin, Strategies for improving the storage performance of silicon-based anodes in lithium-ion batteries, Nano Res. 12 (8) (2019) 1739–1749, http://dx.doi.org/10.1007/s12274-019-2361-4.

[14] H. Kim, M. Seo, M.-H. Park, J. Cho, A critical size of silicon nano-anodes for lithium rechargeable batteries, Angew. Chem., Int. Ed. Engl. 49 (12) (2010) 2146–2149, http://dx.doi.org/10.1002/anie.200906287.

[15] Y. Yang, W. Yuan, W. Kang, Y. Ye, Y. Yuan, Z. Qiu, C. Wang, X. Zhang, Y. Ke, Y. Tang, Silicon-nanoparticle-based composites for advanced lithium-ion battery anodes, Nanoscale 12 (14) (2020) 7461–7484, http://dx.doi.org/10.1039/C9NR10652A.

[16] C.K. Chan, H. Peng, G. Liu, K. McIlwrath, X.F. Zhang, R.A. Huggins, Y. Cui, High-performance lithium battery anodes using silicon nanowires, Nature Nanotechnol. 3 (1) (2008) 31–35, http://dx.doi.org/10.1038/nnano.2007.411.

[17] N. Liu, L. Hu, M.T. McDowell, A. Jackson, Y. Cui, Prelithiated silicon nanowires as an anode for lithium ion batteries, ACS Nano 5 (8) (2011) 6487–6493, http://dx.doi.org/10.1021/nn2017167.

[18] M.-H. Park, M.G. Kim, J. Joo, K. Kim, J. Kim, S. Ahn, Y. Cui, J. Cho, Silicon nanotube battery anodes, Nano Lett. 9 (11) (2009) 3844–3847, http://dx.doi.org/10.1021/nl902058c.

[19] M. Cui, L. Wang, X. Guo, E. Wang, Y. Yang, T. Wu, D. He, S. Liu, H. Yu, Designing of hierarchical mesoporous/macroporous silicon-based composite anode material for low-cost high-performance lithium-ion batteries, J. Mater. Chem. A 7 (8) (2019) 3874–3881, http://dx.doi.org/10.1039/C8TA11684A.

[20] H. Li, X. Huang, L. Chen, G. Zhou, Z. Zhang, D. Yu, Y.J. Mo, N. Pei, The crystal structural evolution of nano-Si anode caused by lithium insertion and extraction at room temperature, Solid State Ion. 135 (1–4) (2000) 181–191, http://dx.doi.org/10.1016/S0167-2738(00)00362-3.

[21] J. Wang, T. Xu, X. Huang, H. Li, T. Ma, Recent progress of silicon composites as anode materials for secondary batteries, Rsc Adv. 6 (90) (2016) 87778–87790, http://dx.doi.org/10.1039/C6RA08971B.

[22] F. Dou, L. Shi, G. Chen, D. Zhang, Silicon/carbon composite anode materials for lithium-ion batteries, Electrochem. Energy Rev. 2 (1) (2019) 149–198, http://dx.doi.org/10.1007/s41918-018-00028-w.

[23] X. Shen, Z. Tian, R. Fan, L. Shao, D. Zhang, G. Cao, L. Kou, Y. Bai, Research progress on silicon/carbon composite anode materials for lithium-ion battery, J. Energy Chem. 27 (4) (2018) 1067–1090, http://dx.doi.org/10.1016/j.jechem.2017.12.012.

[24] A.M. Escamilla-Pérez, A. Roland, S. Giraud, C. Guiraud, H. Virieux, K. Demoulin, Y. Oudart, N. Louvain, L. Monconduit, Pitch-based carbon/nano-silicon composite, an efficient anode for li-ion batteries, RSC Adv. 9 (19) (2019) 10546–10553, http://dx.doi.org/10.1039/C9RA00437H.

[25] Y. Zhu, J. Li, M.S. Saleh, H. Pham, T.P. Plateau, R. Panat, J. Park, Towards high-performance Li-ion batteries via optimized three-dimensional micro-lattice electrode architectures, J. Power Sources 476 (2020) 228593, http://dx.doi.org/10.1016/j.jpowsour.2020.228593.

[26] T.S. Arthur, D.J. Bates, N. Cirigliano, D.C. Johnson, P. Malati, J.M. Mosby, E. Perre, M.T. Rawls, A.L. Prieto, B. Dunn, Three-dimensional electrodes and battery architectures, MRS Bull. 36 (7) (2011) 523–531, http://dx.doi.org/10.1557/mrs.2011.156.

[27] J. Li, M.C. Leu, R. Panat, J. Park, A hybrid three-dimensionally structured electrode for lithium-ion batteries via 3D printing, Mater. Des. 119 (2017) 417–424, http://dx.doi.org/10.1016/j.matdes.2017.01.088.

[28] L. Li, H. Tan, X. Yuan, H. Ma, Z. Ma, Y. Zhao, J. Zhao, X. Wang, D. Chen, Y. Dong, Direct ink writing preparation of LiFePO$_4$/MWCNTs electrodes with high-areal Li-ion capacity, Ceram. Int. 47 (15) (2021) 21161–21166, http://dx.doi.org/10.1016/j.ceramint.2021.04.119.

[29] A. Maurel, S. Grugeon, B. Fleutot, M. Courty, K. Prashantha, H. Tortajada, M. Armand, S. Panier, L. Dupont, Three-dimensional printing of a LiFePO$_4$/graphite battery cell via fused deposition modeling, Sci. Rep. 9 (1) (2019) 1–14, http://dx.doi.org/10.1038/s41598-019-54518-y.

[30] Y. He, S. Chen, L. Nie, Z. Sun, X. Wu, W. Liu, Stereolithography three-dimensional printing solid polymer electrolytes for all-solid-state lithium metal batteries, Nano Lett. 20 (10) (2020) 7136–7143, http://dx.doi.org/10.1021/acs.nanolett.0c02457.

[31] L.J. Deiner, T. Jenkins, A. Powell, T. Howell, M. Rottmayer, High capacity rate capable aerosol jet printed li-ion battery cathode, Adv. Eng. Mater. 21 (5) (2019) 1801281, http://dx.doi.org/10.1002/adem.201801281.

[32] C.C. Ho, K. Murata, D.A. Steingart, J.W. Evans, P.K. Wright, A super ink jet printed zinc-silver 3D microbattery, J. Micromech. Microeng. 19 (9) (2009) 094013, http://dx.doi.org/10.1088/0960-1317/19/9/094013.

[33] R. Noguera, M. Lejeune, T. Chartier, 3D fine scale ceramic components formed by ink-jet prototyping process, J. Eur. Ceram. Soc. 25 (12) (2005) 2055–2059, http://dx.doi.org/10.1016/j.jeurceramsoc.2005.03.223.

[34] B. Derby, N. Reis, Inkjet printing of highly loaded particulate suspensions, MRS Bull. 28 (11) (2003) 815–818, http://dx.doi.org/10.1557/mrs2003.230.

[35] Fujifilm, Printhead reference chart PDS00015, 2022, https://asset.fujifilm.com/www/nl/files/2020-03/171afe178b58bf4b7833bf9435b81c27/PDS00015.pdf. (Accessed 20 December 2022).

[36] M. Pei, H. Shi, F. Yao, S. Liang, Z. Xu, X. Pei, S. Wang, Y. Hu, 3D printing of advanced lithium batteries: a designing strategy of electrode/electrolyte architectures, J. Mater. Chem. A 9 (45) (2021) 25237–25257, http://dx.doi.org/10.1039/D1TA06683H.

[37] S. Arora, A.T. Abkenar, S.G. Jayasinghe, K. Tammi, Chapter 4 - Materials and manufacturing methods for advanced li-ion batteries, in: Heavy-Duty Electric Vehicles, Butterworth-Heinemann, 2021, pp. 69–104, http://dx.doi.org/10.1016/B978-0-12-818126-3.00007-5.

[38] Y. Yang, W. Yuan, X. Zhang, Y. Yuan, C. Wang, Y. Ye, Y. Huang, Z. Qiu, Y. Tang, Overview on the applications of three-dimensional printing for rechargeable lithium-ion batteries, Appl. Energy 257 (2020) 114002, http://dx.doi.org/10.1016/j.apenergy.2019.114002.

[39] K. Sztymela, M. Bienia, F. Rossignol, S. Mailley, S. Ziesche, J. Varghese, M. Cerbelaud, Fabrication of modern lithium ion batteries by 3D inkjet printing: opportunities and challenges, Heliyon (2022) e12623, http://dx.doi.org/10.1016/j.heliyon.2022.e12623.

[40] B. Derby, Additive manufacture of ceramics components by inkjet printing, Engineering 1 (1) (2015) 113–123, http://dx.doi.org/10.15302/J-ENG-2015014.

[41] G.H. McKinley, M. Renardy, Wolfgang von Ohnesorge, Phys. Fluids 23 (12) (2011) 127101, http://dx.doi.org/10.1063/1.3663616.

[42] G. Vescio, J. López-Vidrier, R. Leghrib, A. Cornet, A. Cirera, Flexible inkjet printed high-k HfO$_2$-based MIM capacitors, J. Mater. Chem. C 4 (9) (2016) 1804–1812, http://dx.doi.org/10.1039/C5TC03307A.

[43] S. Subramanian, G. Øye, Aqueous carbon black dispersions stabilized by sodium lignosulfonates, Colloid Polym. Sci. 299 (7) (2021) 1223–1236, http://dx.doi.org/10.1007/s00396-021-04840-7.

[44] C.G. Kolb, M. Lehmann, J.-L. Lindemann, A. Bachmann, M.F. Zaeh, Improving the dispersion behavior of organic components in water-based electrode dispersions for inkjet printing processes, Appl. Sci. 11 (5) (2021) 2242, http://dx.doi.org/10.3390/app11052242.

[45] J.-S. Bridel, T. Azais, M. Morcrette, J.-M. Tarascon, D. Larcher, Key parameters governing the reversibility of Si/carbon/CMC electrodes for Li-ion batteries, Chem. Mater. 22 (3) (2010) 1229–1241, http://dx.doi.org/10.1021/cm902688w.

[46] A. Roland, J. Fullenwarth, J.-B. Ledeuil, H. Martinez, N. Louvain, L. Monconduit, How carbon coating or continuous carbon pitch matrix influence the silicon electrode/electrolyte interfaces and the performance in Li-ion batteries, Battery Energy 1 (1) (2022) 20210009, http://dx.doi.org/10.1002/bte2.20210009.

[47] Y. Li, O. Dahhan, C.D. Filipe, J.D. Brennan, R.H. Pelton, Optimizing piezoelectric inkjet printing of silica sols for biosensor production, J. Sol-Gel Sci. Technol. 87 (2018) 657–664, http://dx.doi.org/10.1007/s10971-018-4762-3.

[48] Y. Li, O. Dahhan, C.D. Filipe, J.D. Brennan, R.H. Pelton, Deposited nanoparticles can promote air clogging of piezoelectric inkjet printhead nozzles, Langmuir 35 (16) (2019) 5517–5524, http://dx.doi.org/10.1021/acs.langmuir.8b04335.

[49] N.F. Morrison, O.G. Harlen, Viscoelasticity in inkjet printing, Rheol. Acta 49 (2010) 619–632, http://dx.doi.org/10.1007/s00397-009-0419-z.

[50] G. Mussabek, S.A. Alekseev, A.I. Manilov, S. Tutashkonko, T. Nychyporuk, Y. Shabdan, G. Amirkhanova, S.V. Litvinenko, V.A. Skryshevsky, V. Lysenko, Kinetics of hydrogen generation from oxidation of hydrogenated silicon nanocrystals in aqueous solutions, Nanomaterials 10 (7) (2020) 1413, http://dx.doi.org/10.3390/nano10071413.

[51] D.B. Mawhinney, J.A. Glass, J.T. Yates, FTIR study of the oxidation of porous silicon, J. Phys. Chem. B 101 (7) (1997) 1202–1206, http://dx.doi.org/10.1021/jp963322r.

[52] K.N. Al-Milaji, H. Zhao, New Perspective of mitigating the coffee-ring effect: Interfacial assembly, J. Phys. Chem. C 123 (19) (2019) 12029–12041, http://dx.doi.org/10.1021/acs.jpcc.9b00797.